MIT Libraries | DSpace@MIT

MIT Open Access Articles

Low-Thrust Solid Rocket Motors for Small, Fast Aircraft Propulsion: Design and Development

Massachusetts Institute of Technology

Low thrust solid rocket motors for small, fast aircraft propulsion: design and development

Matthew T. Vernacchia[*], Kelly J. Mathesius[†] and R. John Hansman[‡]

Massachusetts Institute of Technology, Cambridge, Massachusetts, 02139

Small, low-thrust, long-burn-time solid propellant rocket motors could provide propulsion for a new class of kilogram-scale, transonic uncrewed aerial vehicles (UAVs). This paper investigates technological challenges of small, low-thrust solid rocket motors: slow-burn solid propellants, motors which have low thrust relative to their size (and thus have low chamber pressure), thermal protection for the motor case, and small nozzles which can withstand long burn times. Slow-burn propellants were developed using ammonium perchlorate and 0–20% oxamide (burn rate suppressant), with burn rates of 1–4 mm s^{-1} at 1 MPa. Using these propellants, a low-thrust motor successfully operated at a thrust / burn area ratio 10 times less than that of typical solid rocket motors. This kilogram-scale motor can provide 5–10 N of thrust for 1–3 minutes. An ablative thermal protection liner was tested in these firings, and a new ceramic-insulated nozzle was demonstrated. This paper shows that small, low-thrust solid motors are feasible, and presents a baseline design for the integration of such a motor into a small UAV.

Nomenclature

a	=	Propellant burn rate coefficient [m s^{-1} Pa^{-n}]
A_b	=	Area of burning propellant surface [m^2]
A_t	=	Nozzle throat area [m^2]
A_w	=	Exposed wall area [m^2]
c^*	=	Characteristic velocity of the propellant/motor [m s^{-1}]
C_D	=	Aircraft drag coefficient [dimensionless]
C_F	=	Thrust coefficient of the rocket motor [dimensionless]
$C_{geometry}$	=	Geometric factor in thermal stress model [dimensionless]
C_{soot}	=	Soot concentration by volume in the exhaust gas [dimensionless]
c_p	=	Specific heat capacity of the combustion gas [J kg^{-1} K^{-1}]

*Graduate student, Department of Aeronautics and Astronautics, AIAA student member.

†Graduate student, Department of Aeronautics and Astronautics, AIAA student member.

‡T. Wilson Professor in Aeronautics, Department of Aeronautics and Astronautics, AIAA member

E	=	Elastic modulus [Pa]
F	=	Thrust force of the rocket motor [N]
$h_{external}$	=	Convection coefficient of external airflow [W m^{-2} K^{-1}]
I_{sp}	=	Specific impulse [s]
k_{virign}	=	Thermal conductivity of the virgin ablative material [W m^{-1} K^{-1}]
k_{insul}	=	Thermal conductivity of fiberglass insulation behind the ablative material [W m^{-1} K^{-1}]
$\dot{m}$	=	Mass flow rate [kg s^{-1}]
m_p	=	propellant grain mass [kg]
n	=	Propellant burn rate exponent [dimensionless]
p_c	=	Chamber pressure of the motor [Pa]
q	=	Dynamic pressure of external air flow [Pa]
q_{conv}	=	Convective heat flux to the wall [W m^{-2}]
q_{rad}	=	Radiative heat flux to the wall [W m^{-2}]
r	=	Propellant burn rate [m s^{-1}]
Re_D	=	Reynolds number, with passage diameter as length scale [dimensionless]
R_s	=	Thermal shock resistance parameter [K]
S_{flex}	=	Flexural strength [Pa]
S_{ref}	=	Aircraft drag reference area (fuselage frontal area) [m^2]
St	=	Stanton number [dimensionless]
T_{aw}	=	Adiabatic wall temperature [K]
T_g	=	Gas temperature [K]
T_w	=	Wall temperature [K]
α_{LE}	=	Coefficient of thermal expansion (linear) [K^{-1}]
ϵ_g	=	Total emittance of the gas [dimensionless]
ϵ_{case}	=	Emissivity of the motor case outer surface [dimensionless]
ν	=	Poisson's ratio [dimensionless]
ρ_g	=	Density of the combustion gas [kg m^{-3}]
ρ_s	=	Solid density of the propellant [kg m^{-3}]
σ_{SB}	=	Stefan-Boltzmann constant [W m^{-2} K^{-4}]
σ_θ	=	Hoop stress [Pa]
ζ_{C_F}, ζ_{c^*}	=	C_F, c^* efficiency (measured / ideal values) [dimensionless]

I. Introduction

A. Motivation: the small and fast aircraft capability gap

A gap exists in the size and capability of flight vehicles: no small vehicles are capable of sustained level flight at high speed. There is an undeveloped regime of aircraft with speed above $100\,\mathrm{m\,s^{-1}}$ and mass below $10\,\mathrm{kg}$, based on a survey of US military aircraft specifications in [1–3]. Small, fast aircraft in this regime would be a useful extension of existing capabilities. The proposed aircraft would be carried by a larger host aircraft and air-launched near its cruise speed and altitude.

One significant challenge is that small, fast aircraft need propulsion systems with high energy density: as an aircraft is made smaller, the volume for energy storage ($\sim$ (length scale)^3) shrinks faster than the power demand ($\sim$ (drag) $\sim$ (length scale)^2). Most small aircraft currently use electrically-powered propellers; however, the low energy density of batteries makes electric aircraft unsuited for sustained flight at high speeds. Turbine engines and solid rocket motors have the requisite energy and power density, but turbine engines are mechanically complex and difficult to miniaturize. Solid rocket motors offer high specific power and low mechanical complexity.

Small, fast aircraft have different thrust and endurance requirements than typical applications of solid rocket motors: the rocket motor must deliver a low thrust level, just enough to counter drag, for a few minutes. In contrast, typical solid rockets deliver their impulse quickly, either to catch up with a target (i.e. tactical missiles) or reduce gravity losses (i.e. sounding rockets and launch vehicles). Most kilogram-scale solid rocket motors only burn for a few seconds, not minutes. Further, the motors investigated here have thrust levels which are unusually low, even relative to the size of the motor. The thrust / burn area ratio is a measure of thrust relative to motor size; these motors have thrust / burn area ratio 1/10th that of typical solid rocket motors. Adapting solid rockets to the needs of small, fast aircraft is the focus of this paper.

B. Previous research on low-thrust, long-burn-time rocket motors

The key design principles for low-thrust, long-burn-time solid rocket motors are to reduce the propellant burn area A_b by using an end-burn grain, to reduce the propellant burn rate by using large AP particles or burn rate suppressants such as oxamide, and to operate at low chamber pressure [4]. Among the first designs to employ these principles were a series of long-burn-time demonstration motors tested at JPL from 1969-1971 [5]. These motors produced roughly $8\,\mathrm{kN}$ of thrust for 110–138 s, at chamber pressures of only 0.8–1.0 MPa. More recently, Nowakowski *et al.* [6] proposed a $245\,\mathrm{N}$ thrust, 324 s burn-time motor using these techniques.

Perhaps the most similar motor to those considered here is the "Five-Minute Rocket Motor" developed by Atlantic Research Corporation in the 1970s [7]. Producing $200\,\mathrm{N}$ of thrust for 290 s, this motor was also designed for aircraft propulsion. It had a diameter of 178 mm and a total total mass of 53 kg. It used an end-burn propellant grain, with the burn rate reduced by adding 5% by mass oxamide to the propellant, and had a chamber pressure of 2.4 MPa. The

thermal challenge of a long duration end-burn motor was addressed by lining the motor case with a composite ablative.

The motors considered here are considerably smaller, with total mass on the order of 1 kg and thrust on the order of 10 N. Nonetheless, the key design principles of an end-burn grain, slow-burn propellant and low chamber pressure are still applicable. This paper incrementally extends these approaches to higher oxamide contents (up to 20%) and lower chamber pressures (down to 0.5 MPa), and quantifies the lower limits on thrust / burn area possible with these techniques. It also reports new challenges with combustion gas heat loss and nozzle insulation, which only occur at small sizes and were not reported in the previous studies of long-burn-time motors.

II. Design of small, low-thrust motors

A. Design goals: range and endurance

The influence of the propulsion system on range can be understood from the Bréguet range equation [8]. To maximize range, the motor should be long and slender to reduce the fuselage drag, the motor should have high specific impulse I_{sp}, and the motor's inert mass fraction should be low, to give the aircraft higher $\frac{m_{initial}}{m_{final}}$. Figure 1 uses the Bréguet equation to show the powered range of a hypothetical aircraft using such a motor (blue dashed curve), compared against a conventional ballistic rocket (black curve). Both vehicles have an initial mass of 3 kg and are launched at 10 km altitude and 239 m s^{-1} (Mach 0.8). The aircraft cruises at that speed, and has a lift to drag ratio of 4. The conventional ballistic rocket uses a higher-thrust motor that burns for only a few seconds, quickly accelerates to supersonic speeds, and has an initial 45° flight path angle*. As the ballistic rocket is un-powered for most of its flight, its range is more properly compared to the powered plus glide range of the aircraft (solid blue curve). For propellant mass fractions up to 0.5, the aircraft has longer range-to-ground-impact than the ballistic rocket, on the order of 40–100 km. Beyond the range comparison, the rocket-propelled aircraft also offers very different trajectory options.

B. Aircraft and motor configuration, notional mission

A proposed aircraft and rocket motor configuration is shown in fig. 2. The fuselage is long and slender, with tapered ends, to reduce drag. The motor case is the primary structure of the fuselage and has a circular cross section using high strength/density material (e.g. titanium alloy Ti-6Al-4V) to reduce inert mass.

An end-burn grain is chosen to give a small propellant burn area, low thrust, and long burn time. An ablative material lines the inside of the motor case to protect the motor case from the hot combustion gas; still, the aft end of the motor case is expected to reach 500–650 K (see fig. 7). The payload and controls are mounted to the front of the motor case, which remains cooler.

The nozzle is mounted into the tapered aft end of the motor case (fig. 2, right side). Because of its small size, the nozzle cannot use ablative cooling, which would give unacceptable erosion of the nozzle contour. To keep the

---

*The ballistic rocket's range is computed using an ODE solver, a generic streamlined body $C_D(M)$ table, and the COESA atmosphere model.
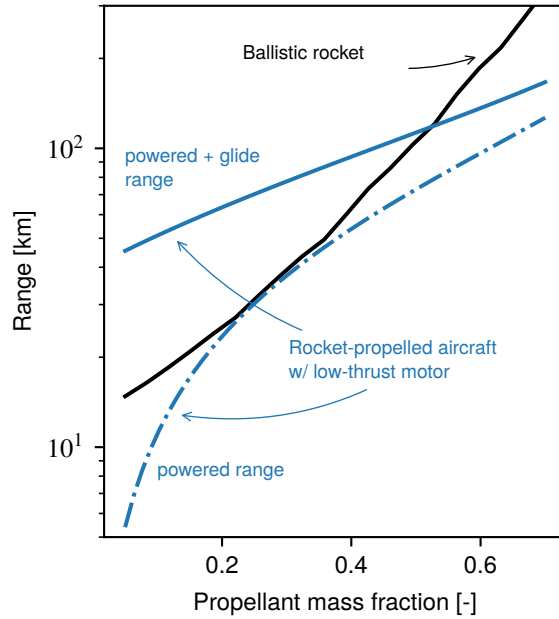
Fig. 1 Notional range of a small aircraft using the low-thrust rocket motor proposed in this work (8 N thrust, 110 s I_{sp}, blue curves), compared to a same-size ballistic rocket using a typical high-thrust motor (200 N thrust, 220 s I_{sp}, black curve).

motor case at an acceptable temperature, the nozzle is supported by special ceramic insulation. Because of the large temperature variations, material selection must be carefully considered: both the nozzle insert material, boron nitride, and the insulation, fused silica, are highly resistant to thermal shock.
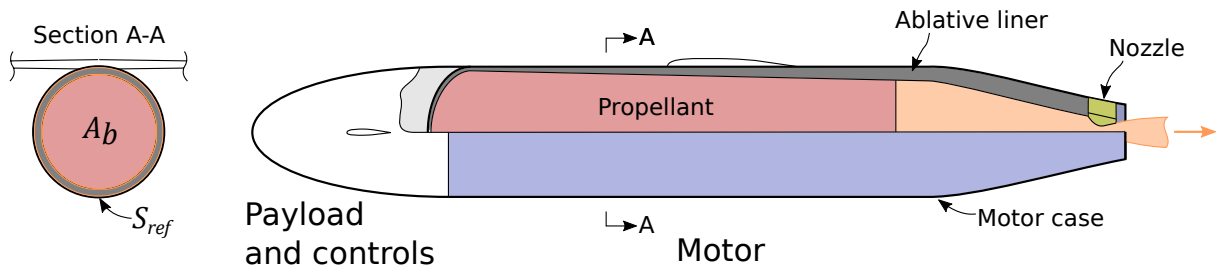

Fig. 2 Concept for a small, fast rocket-propelled aircraft: configuration and motor components. Many configurations of the aerodynamic surfaces are possible, one option is shown in white outlines.

To illustrate this configuration, an example aircraft's notional mission requirements are given in table 1 and notional design parameters are given in table 2. The exact thrust level depends on details of the aerodynamic design and mission; it can be set by adjusting the amount of burn rate suppressant in the propellant and the nozzle throat diameter. With a fixed propellant burn area, a smaller nozzle throat area would raise the chamber pressure, make the propellant burn more quickly, and increase thrust.

Table 1 Notional requirements for an example small, fast aircraft using rocket propulsion.

Parameter	Value
Launch altitude	10 km
Cruise speed	Mach 0.8
Payload	300 g

Table 2 Notional design parameters of a low thrust rocket motor for the example aircraft/mission.

Parameter	Value
Thrust	5–10 N
Burn time	100–200 s
Total impulse	1100 N s
I_{sp}, delivered	110 s
Chamber pressure	0.5–2 MPa
Propellant mass	1 kg
Propellant	AP + HTPB + oxamide (0-20% by mass)
Case diameter	70 mm
Nozzle throat diameter	2–5 mm

C. Aircraft and motor design coupled via the thrust / burn area ratio

The thrust / burn area ratio, F/A_b, is a useful parameter for examining the link between the aircraft configuration, flight conditions, and motor design. For the example mission (table 1), thrust and burn area are fixed by the aircraft design and desired trajectory, and set a F/A_b ratio which is 1/10th the value of typical solid rocket motors. Figure 3 shows the F/A_b needed for rocket-propelled aircraft and table 3 gives F/A_b for typical rocket motors.

For steady, level flight, thrust is set to match the drag on the aircraft at cruise speed: $F = D = qC_D S_{ref}$, where the drag reference area S_{ref} is chosen to be the forward-facing area of the fuselage. Dividing both sides by A_b gives:

$$\frac{F}{A_b} = qC_D \left(\frac{S_{ref}}{A_b}\right) \tag{1}$$

Here, the dynamic pressure q depends on the trajectory, and S_{ref}/A_b depends on how the motor is configured within the fuselage. For an end-burn motor, A_b is the transverse section area of the propellant grain, and S_{ref} will be slightly larger, due to the ablative liner and case wall which surround the propellant (fig. 2).

A simple model is used to illustrate the trends in required F/A_b versus cruise altitude and Mach number; the results are shown in fig. 3. F/A_b is computed from eq. (1), with $q = (\gamma_{\text{air}}/2)p_a M^2$. p_a vs. altitude is from the COESA atmosphere model (left inset), and a generic transonic drag rise curve is used for C_D vs. Mach (bottom inset).

Typical solid rocket motors operate at $F/A_b > 15$ kPa (see table 3). Most of the cruise conditions in fig. 3 require much lower F/A_b. The contours in fig. 3 cover the range of F/A_b (2–15 kPa) supported by the low-thrust motors
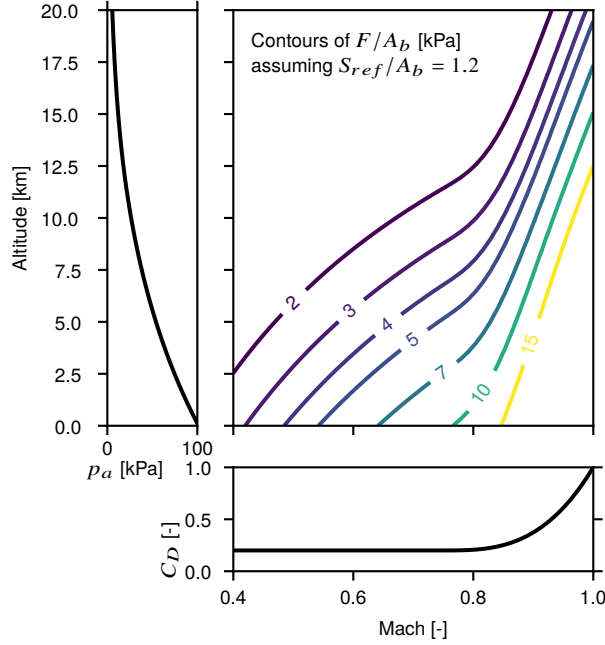
Fig. 3   Contours of required F/A_b for steady, level flight versus cruise altitude and Mach number. F/A_b is computed from eq. (1), using the atmospheric pressure and drag models shown in the inset plots.

proposed here. As will be discussed below, even these motors cannot achieve F/A_b much below 2 kPa.

To derive the relation of F/A_b to the other motor design parameters, we start with the equations for thrust[†] and mass flow equilibrium (see Sutton and Biblarz [4]): $F = p_c A_t C_F(p_c)$ and $\dot{m} = p_c A_t/c^* = A_b r \rho_s = A_b(a p_c^n)\rho_s$. Combining the two equations gives:

$$\frac{F}{A_b} = p_c^n C_F(p_c) c^* a \rho_s \tag{2}$$

The F/A_b ratio depends on the chamber pressure and the properties of the propellant (n, c^*, a and ρ_s). F/A_b does not depend on the size of the motor. In fact, table 3 shows that several motors, which differ in size (total impulse) by five orders of magnitude, have similar values of F/A_b, all between 15 kPa and 35 kPa. However, as shown in fig. 3, low-thrust motors for small, fast aircraft need much lower F/A_b.

To make F/A_b small, the motor must operate at low p_c and use a slow-burn propellant with low a. This motivated the development of slow-burn propellants for use at low chamber pressures, described in an accompanying paper [9]. However, operating at low p_c reduces C_F and I_{sp} because the nozzle expansion is less efficient with a lower pressure ratio across the nozzle. Also, each propellant has a minimum pressure below which it will not burn. These considerations set lower limits on F/A_b.

This trend is illustrated in fig. 4 for several different propellants. For each propellant, F/A_b is calculated using

---

[†]Properly, C_F is a function of γ, p_e/p_c, and p_a/p_c. In this analysis, it is assumed that γ is the same for all propellants, and that the nozzle expansion is always designed to give p_e matched to the ambient pressure at the cruise altitude. With these other parameters fixed, C_F is a function of just p_c.

Table 3 Different solid rocket motors, with a wide range of sizes and applications, all operate at similar F/A_b. Thrust and burn area are average values over the burn time. All these motors use ammonium perchlorate composite propellant and core-burning grains. Cesaroni data from manufacturer's specifications and measurement of propellant grains, other data from [4].

Motor	Application	Thrust [N]	Burn area [m^2]	F/A_b [kPa]
First Stage, Minuteman	Missile booster	865 581	24.84	34.8
Orbus-6	Upper stage	76 394	2.52	30.3
STAR 27	Upper stage	26 732	0.89	30.1
Cesaroni P38-6G Classic	Hobby	325.3	0.0204	15.9
Cesaroni P38-2G Classic	Hobby	125.1	0.0068	18.4

eq. (2). The propellant properties in eq. (2) are taken from Vernacchia *et al.* [9]. I_{sp} is calculated using the ideal 1d nozzle model, assuming matched expansion to an ambient pressure of 30 kPa. Three propellants are ammonium perchlorate (AP) propellants developed in [9]. In these propellants, the burn rate is set by the amount of oxamide (a burn rate suppressant); propellants with more oxamide burn more slowly at a given pressure. For comparison, an ammonium nitrate (AN) propellant is also included in fig. 4; properties are from [4] and experiments in [10].
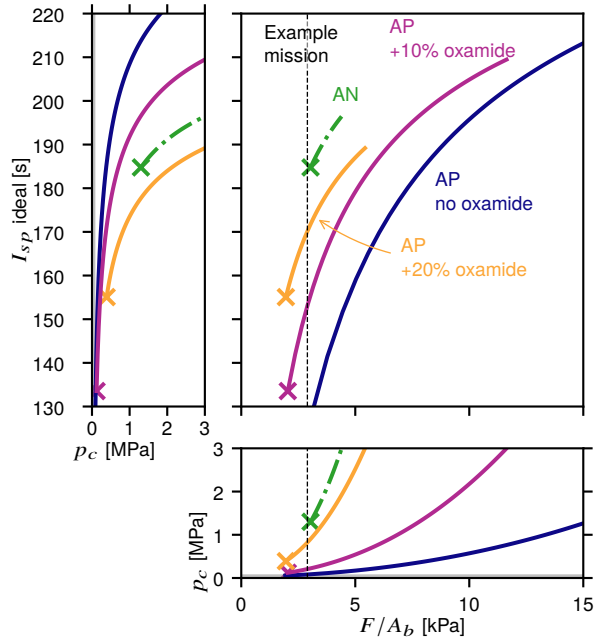

Fig. 4 Operating at lower F/A_b reduces specific impulse. Slower-burning propellants give higher specific impulse at a given F/A_b.

For each propellant, lower p_c reduces I_{sp} (left inset), and achieving lower F/A_b requires lower p_c (bottom inset). Thus, for each propellant, the achievable I_{sp} is lower if the required F/A_b is lower (top-right plot). The minimum combustion pressures for each propellant are marked with an 'x'. The AP baseline propellant curve is not marked with

an 'x' because the minimum p_c to choke the nozzle flow is higher than the minimum burn pressure of this propellant. The minimum burn pressures were measured in a strand burner, as detailed in [9]. The minimum burn pressure sets a minimum F/A_b for each propellant.

Although the AN propellant has the slowest burn rate, the AP+oxamide propellants can operate at lower F/A_b because they have lower minimum combustion pressures. The 10% and 20% oxamide propellants both can provide F/A_b down to about 2 kPa.

At a given chamber pressure, propellants with lower c^* give lower I_{sp} (left inset). For the AP+oxamide propellants, adding more oxamide reduces the flame temperature and decreases c^*. At a given F/A_b, the slower-burning propellants can operate at a higher chamber pressure (bottom inset). At a given F/A_b, slower-burning propellants give higher I_{sp} (top-right plot), because the effect of higher chamber pressure outweighs the lower c^*.

The F/A_b required for the example mission (table 1) is about 2.9 kPa and is marked with a black dotted line. At this F/A_b, the baseline AP propellant would need such a low p_c that the nozzle flow would barely reach sonic velocity, and the specific impulse would be very low ($I_{sp}^{ideal} < 130$ s). The 10% and 20% oxamide propellants can operate at the example mission F/A_b. For the 10% oxamide propellant, the motor would operate at $p_c = 0.21$ MPa and $I_{sp}^{ideal} = 153$ s; for the 20% oxamide propellant, $p_c = 0.81$ MPa and $I_{sp}^{ideal} = 170$ s. Practically, the desired chamber pressure would be achieved by setting the A_b/A_t ratio of the motor, and the throat areas would be different for the different propellants.

For $F/A_b > 3.1$ kPa, the AN propellant can operate and has slightly higher specific impulse than the AP+oxamide propellant (fig. 4, top-right). However, the AN propellant is less dense (1480 kg m^{-3} vs. 1600 kg m^{-3}) so less propellant mass can fit in the motor. Additionally, the AP+oxamide propellant family can be used for a wider range of F/A_b. Thus, the AP+oxamide propellants are preferred for this application.

III. Motor case and nozzle thermal protection challenges

A. Motor case design and thermal protection challenges

The baseline motor case is designed to be simple, lightweight, strong, and manufacturable. Its geometry is a straight cylinder with a domed forward closure and a conical (boat-tail) aft section (fig. 2). The motor case material must have sufficient strength at the maximum expected temperature of 500–650 K (see fig. 7) to support the internal pressure loads, and should have a low density to reduce the motor's inert mass fraction. These requirements suggest a titanium alloy such as Ti-6Al-4V. Low-alloy steels (e.g. D6AC or 4130) are a heavier but less expensive alternative. Aluminum alloys and plastic-matrix composites are not usable at the expected temperatures.

For manufacturing, the straight section can be made from off-the-shelf tube, whereas the more complex forward closure and aft section can be made via additive manufacturing. The authors worked with Renishaw Canada Ltd. of Mississauga, Ontario to print, proof test, and test fire several motor case aft sections made from Ti-6Al-4V.

For a typical internal burning grain, the propellant insulates the majority of the interior motor case surface from the hot combustion gases during the burn. However, for an end-burning grain, most of the inner surface is exposed to 1500–2200 K combustion gas for several minutes. The inner surface of the motor case is protected by an ablative liner, as is standard design practice for solid rocket motors [11]. An additional insulating layer of fiberglass cloth is included between the ablative and the case to further reduce the motor case temperature. The baseline design uses an ablative liner made from Dowsil 93-104 (formerly Dow-Corning 93-104). This ablative consists of glass, ceramic, and carbon fibers in a silicone rubber matrix; some of its thermal properties are reported in [12]. This ablative liner was tested in a research motor, described further in section IV.

The motor case heat transfer problem can be thought of in three zones. In the innermost zone, heat is radiated and convected from the hot gas to the ablative surface. Second, the ablative undergoes pyrolysis reactions, forming char and gaseous products. Third, outside the pyrolysis zone, heat is conducted through the remaining ablative, fiberglass insulation and metallic motor case, and is rejected to the atmosphere by convection and radiation.

These three zones could be modeled together by software such as *CMA* [13] and *FIAT* [14], but here is treated with separate, simple models that are more intuitive. The internal radiation transfer is simpified by treating the gas and solid surface as isothermal radiators. The outer conduction is simplified by noting that the outside of the pyrolysis zone is at a nearly constant temperature, set by the pyrolysis chemistry. The complex middle pyrolysis zone is not modeled, but the char depth vs. exposure time was measured experimentally.

Heat is transferred from the hot gas to the ablative inner wall by both convection and radiation [15–17]. Radiation is the dominant heat transfer mode in these motors, due to 1) the low combustion gas mass flux which reduces convection, and 2) the soot content of the gas which contributes to radiation. Simplified models were used to assess the convective and radiative heat flux to the walls of a cylinder with hot, sooty gas flowing through it.

The convective heat flux was modeled using the Colburn correlation for turbulent pipe flow [18]. The radiative heat flux was modeled assuming radiation from an isothermal soot cloud to an isothermal black wall; in this model:

$$q_{rad} = \sigma_{SB} \left[\epsilon_g(T{=}T_g) \, T_g^4 - \epsilon_g(T{=}T_w) \, T_w^4 \right] \tag{3}$$

where $\epsilon_g(T)$ is the emittance of the soot cloud, and is estimated as:

$$\epsilon_g(T) = \frac{\int_0^\infty \left[1 - \exp\left(-k_1 C_{soot} L_e \lambda^{-1}\right) \right] e_b(\lambda, T) \, d\lambda}{\sigma T^4} \tag{4}$$

with $k_1 = 6$ and $e_b(\lambda, T)$ being the blackbody spectral emissive power from Planck's Law. The procedure for estimating emittance follows [19] and is detailed in [20], section 8.3.1.2. The emittance depends on the concentration of soot C_{soot} and on the mean optical path length through the cloud $L_e = 0.95D$; for the conditions in the example motor
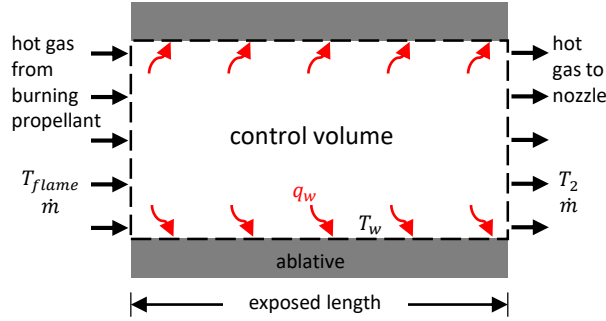
Fig. 5 Control volume for a lumped-parameter model of energy loss from the hot gas.

combustion chamber ($C_{soot} = 10^{-5\ddagger}, D = 60\,\text{mm}$) ϵ_g is expected to be 0.8. Using these models, the radiative heat flux to the chamber walls was predicted to be an order of magnitude greater than the convective heat flux. Thus, only radiative heat flux is considered in the following analysis of hot gas energy loss.

Heat loss to the walls cools the combustion gas before it reaches the nozzle. This decreases the motor's c^* and I_{sp}, as both are proportional to the square root of temperature at the nozzle inlet.

Here, a lumped-parameter model is presented for the cooling of the hot gas by radiation to the walls of the chamber. Consider as a control volume the cylindrical space within the motor between the burning surface of the propellant and the nozzle inlet (fig. 5). Combustion gas enters this volume at the propellant flame temperature T_{flame}, with a mass flow rate $\dot{m}$. It exits this volume into the nozzle at a lower temperature T_2. The char surface surrounding this volume is assumed to be at a uniform and constant temperature T_w, and receives a uniform heat flux q_w.

The conservation of energy equation for this control volume is:

$$\dot{m}c_p(T_{flame} - T_2) = q_w A_w \tag{5}$$

where c_p is the heat capacity of the gas and A_w is the wall area. The heat flux q_w is crudely estimated by treating the gas as an isothermal radiator at an average temperature $T_{avg} = (T_{flame} + T_2)/2$. The heat flux is computed from eq. (3), with T_{avg} substituted for T_g. Cooling will increase the gas density across the control volume, but this effect is neglected when computing the soot concentration and emissivity.

Example results of this model are presented in fig. 6. As the end-burn grain burns away, more length of wall is exposed, and the exposed wall area increases as $A_w = \pi D L_{exposed}$. As A_w increases, more heat is lost and the gas T_2 becomes cooler. The predicted heat loss would reduce the time-averaged c^* efficiency to 0.84, as $\zeta_{c^*} \sim (T_2/T_{flame})^{1/2}$. This severe heat loss is an unusual feature of small, long-burn motors. Because the motor has an end-burning propellant grain, heat radiated from the hot gas is mostly lost to the walls. With a typical core-burning grain, thermal radiation from the hot gas mostly warms the propellant surface; most of the heat is returned to the gas when the propellant burns.

---

‡The soot concentration was measured in separate propellant combustion experiments, see [20], Section 5.6
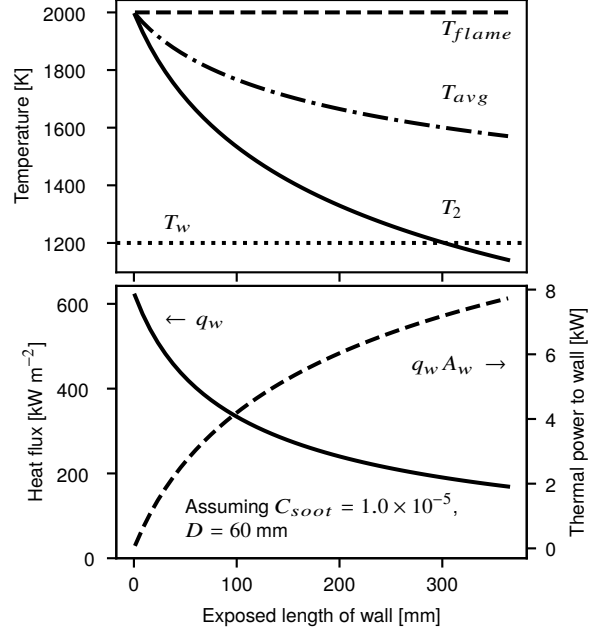
Fig. 6 A model of heat loss from the combustion gas to the walls suggests that the combustion gas will be cooled significantly.

Because the motor is long, small diameter, and operates at low thrust, the ratio $A_w/\dot{m}$ is large. Equation (5) shows that $A_w/\dot{m}$ is proportional to the drop in hot gas temperature. Thus, it seems that low c^* efficiency is an inevitable feature of these motors. This is supported by the c^* measured in static firings (section IV).

For the conduction problem outside the pyrolysis zone, a simple model is used to assess the maximum temperature the motor case could attain at burnout. Imagine that the ablation process were 'paused' at burnout, and the heat transfer from the ablative pyrolysis zone to the motor case came to steady state. The heat flux into the case would be:

$$q_{into\,case,ss} = \left(\frac{l_{virgin}}{k_{virgin}} + \frac{l_{insul}}{k_{insul}} \right)^{-1} (T_{pyrolysis} - T_{case}) \tag{6}$$

where l_{virgin} is the remaining thickness of virgin ablative material, l_{insul} is the fiberglass insulation thickness, and $T_{pyrolysis}$ is the temperature of the pyrolysis zone. The case temperature in this fictional steady state can be found by solving:

$$q_{into\,case,ss} = -q_{external} = h_{external}(T_{case} - T_{air}) + \epsilon_{case}\sigma_{SB}(T_{case}^4 - T_{ambient}^4) \tag{7}$$

In reality, the heat flux into the case will be less than $q_{into\,case,ss}$, because virgin ablative is still warming up. Thus, the solution of eqs. (6) and (7) for T_{case} gives an upper-limit value for the case temperature.

Solutions of this model are plotted versus external convection coefficient in fig. 7. The assumed parameter values are

$l_{virgin} = 1$ mm, $T_{pyrolysis} = 720$ K and $k_{virgin} = 0.35$ W m^{-1} K^{-1} for Dowsil 93-104 [12], $k_{insul} = 0.05$ W m^{-1} K^{-1} [21], $T_{air} = 248$ K, $\epsilon_{case} = 0.3$ (typical for Ti alloys), and $T_{ambient} = 300$ K. The blue region shows the expected range of external airflow convection coefficients in flight. These results give confidence that the motor case will remain below the strength-limit temperature of Ti-6Al-4V, so long as the ablative liner does not char through.
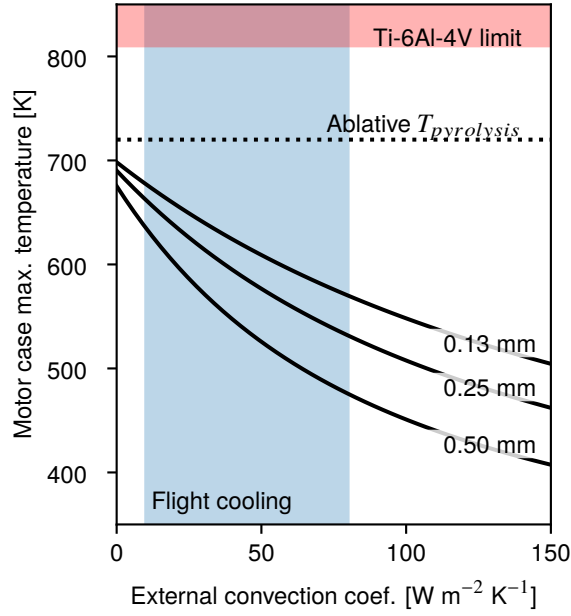

Fig. 7 Upper-limit motor case temperature versus external convection coefficient for several fiberglass insulation thicknesses.

B. Nozzle design and thermal challenges

The size vs. duration design space for solid rocket motor nozzles is shown in fig. 8. The nozzle for the example motor (blue star) is almost alone in the bottom-right corner. Some other motors have similarly small nozzles (e.g. the STAR 4G) but much shorter burn times. Other motors have long burn times (e.g. over 100 s for the Shuttle RSRM, Orbus-21, Condor, and "Five Minute Motor"), but have throat diameters orders of magnitude larger. The bottom-right corner (small, long-burn) of the design space is associated with difficult thermal issues because of the physics of heat transfer within the nozzle.

Conventional solid rocket nozzle designs rely on transient techniques (e.g. heat sink, ablatives). Generally, the length scales for transient heat penetration phenomena (e.g. thermal diffusion, char depth, erosion) scale with exposure time like $t^{1/2}$ to t^{1}. Longer exposure times give length scales which are too large for very small nozzles. For example, a typical ablative nozzle (like the Shuttle RSRM) would erode by 20 mm under the example motor's throat conditions and burn time; however the throat diameter of this nozzle is only 2–5 mm. Instead, a steady-state insulation solution is
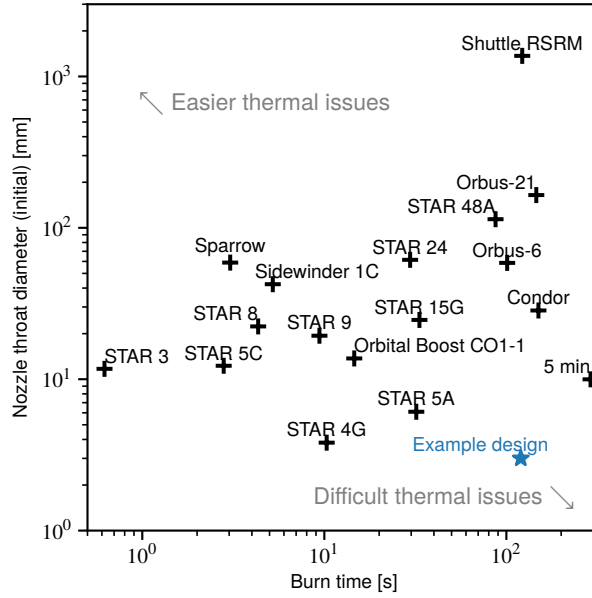
Fig. 8   Design space of nozzle throat diameter vs burn time. Small, long-burn-time nozzles (bottom-right corner of the plot) are unusual and face difficult thermal issues. Data from [4, 7, 22, 23].

proposed.

A representative nozzle design is shown in fig. 9. The nozzle consists of an insert through which the hot gas flows and insulator which contains the heat convected into the insert. The nozzle's structural shell is an extension of the aft section of the motor case. The insert material is boron nitride ceramic and the insulator is fused silica. Because the nozzle shell and insulation have different coefficients of thermal expansion, the shell-insulation bond is made with a flexible silicone adhesive[§].
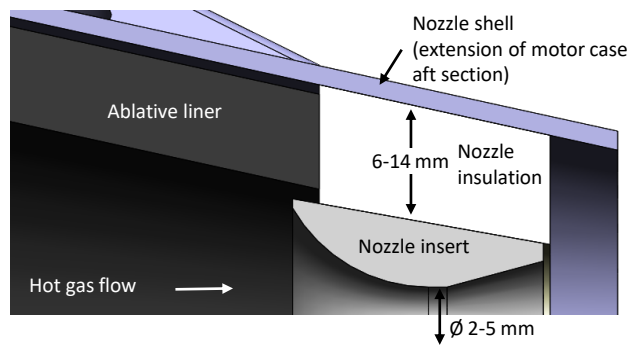

Fig. 9   Section view of the nozzle from the baseline motor design.

Although the insulation is only 6–14 mm thick, there must be a large temperature difference across it. The operating temperature of the insert is 1500–2000 K, whereas the maximum allowable temperature of the shell is limited to 644 K by the shell-insulation adhesive. Thus, the relatively thin insulator must provide a very large thermal resistance, and

---

[§]This work used "Permatex Ultra Copper" RTV silicone from ITW Permatex, Solon, Ohio.

withstand the thermal stresses induced by an extreme thermal gradient.

The thermal expansion of the hot inner material is constrained by the cool outer material. It can be shown [24] that the circumferential tensile stress on the outer surface is:

$$\sigma_\theta = \frac{\alpha_{LE} E}{1 - \nu} \Delta T \, C_{geometry} \tag{8}$$

where ΔT is the temperature difference between the inside and outside of the insulation, and $C_{geometry}$ is a constant factor which depends the insulator geometry.

To survive the thermal stresses, the insulator must be made from a ceramic with favorable material properties. Following Kingery [25], we define the thermal shock resistance parameter R_s:

$$R_s \equiv \frac{S_{flex}(1 - \nu)}{E \alpha_{LE}}; \quad \frac{R_s}{\Delta T} \sim \frac{S_{flex}}{\sigma_\theta} \tag{9}$$

Ceramics with higher R_s will be less likely to fail due to thermal stress. Because the geometry factor in eq. (8) is approximately 1 for the insulator, R_s should (at least) be on the order of the temperature difference ΔT across the insulator. Fused silica is a good insulation material because it has a high R_s (960 K) and low thermal conductivity ($1 \, \mathrm{W \, m^{-1} \, K^{-1}}$).

Insulation with a cellular structure was investigated as a means to further reduce the thermal conductivity and improve the thermal stress resilience. Ceramic materials with a cellular or porous structure are widely used as insulation materials: examples include firebrick, ceramic foam kiln insulation, and silica-fiber Reusable Surface Insulation tiles used on the Space Shuttle Orbiter [26]. For thermal stresses, a cellular structure reduces stiffness (favorable) but also reduces strength (unfavorable); in some cases the net effect increases the thermal shock resistance [27].

The geometry for the cellular insulator is a honeycomb wrapped onto the revolved shape of the insulator (fig. 10). This orientation of the honeycomb gives low stiffness in the circumferential direction at the outer face. When bonded into the motor case, the cells are closed off, and there are multiple solid walls in the axial direction. This gives redundancy against leaks; the insulator will remain gas tight even if a few cell walls crack. The cell wall thickness is just over 1 mm; this is about the thinnest wall that can reliably be produced. The thin cell walls reduce the conductive heat transfer in the radial direction.

This shape is compatible with the vat photo-polymerization[¶] printing process. To produce the insulation, first a green part is printed via vat photopolymerization. The green part consists of silica particles held together by a photopolymer binder. Then, the green part is fired in a kiln to burn out the binder and sinter the particles together. The kiln is held at a maximum temperature of 1271 °C for 5 min; the temperature schedule of the sintering process has important effects on material properties (see [20], section 10.4.1, and [28]). After kiln firing, the fused silica insulation is bonded to the

---

[¶]also known as stereo-lithography (SLA); performed on a Form 2 printer from Formlabs, Somerville, Massachusetts

Small cells reduce
convective heat transfer

Thin walls reduce
conductive heat transfer

Cell walls can flex
to comply with
thermal expansion
in the $r\,\theta$ plane

Section view

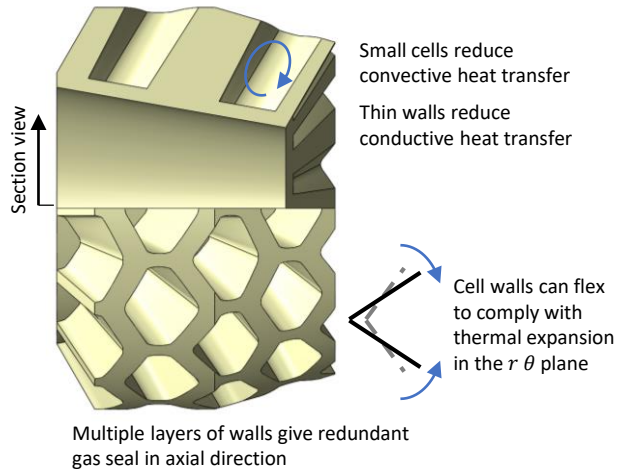Multiple layers of walls give redundant
gas seal in axial direction

Fig. 10   Geometry of the honeycomb cellular ceramic insulation invented for this work.

boron nitride nozzle insert using a silica ceramic adhesive. The insulation and insert are then bonded into the nozzle shell with a silicone polymer adhesive.

Analysis of the thermal stresses in the honeycomb (presented in [20], section 10.3, using honeycomb mechanics theory from [29]) indicates that the thermal stresses in the honeycomb are less if the cell walls are thinner. At the current minimum printable wall thickness (1 mm), the honeycomb does not have better thermal stress performance than a monolith. However, finer walls and better thermal stress performance may become possible as printing technology improves. Because the cellular design offers other advantages (lower thermal conductivity, limited crack propagation, and better binder burn-out during sintering), it was selected as the baseline insulation design.

Thermal analysis was conducted to determine the insulation thickness required to keep the nozzle shell temperature below the temperature limit of the shell-insulator adhesive (fig. 11). A 2d axi-symmetric, steady state, finite element model was used. The internal convection boundary condition was determined in a separate CFD analysis (detailed in [20], section 9.2.1.3), which accounted for film cooling from the ablative liner and used a hot gas temperature of 2000 K and pressure of 0.7 MPa. Increasing the hot gas temperature or pressure would cause the shell temperature to be higher than shown in fig. 11. The external boundary condition assumed convection with $T_{aw} = 248$ K, and radiation with $\epsilon = 0.9$ to a 300 K environment. The exact external convection coefficient will depend on the flight altitude, speed and detailed aerodynamic design, but a plausible range is highlighted in blue in fig. 11. An insulation thickness of 10 mm is expected to suffice for most conditions. Thicker insulation increases the base diameter of the fuselage, which increases drag and decreases range.

C. Nozzle clogging and pressure spikes

The nozzle is vulnerable to clogging by solid debris, due to its very small throat size. Several temporary 'spikes' in chamber pressure were observed in the motor firings. These spikes had amplitudes of 0.09–1 MPa above the earlier
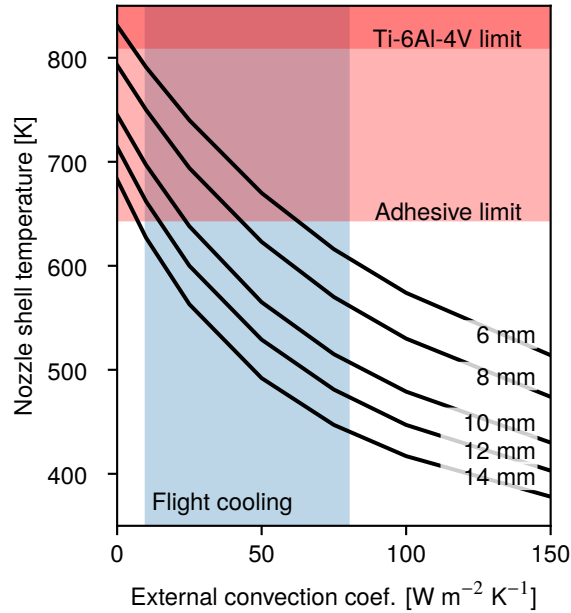
Fig. 11 Maximum steady-state temperature on the nozzle shell versus external convection coefficient for various nozzle insulation thicknesses.

chamber pressure (10-100% of nominal chamber pressure at time of excursion) and rise times of about 1 s (pressure traces from the motor firings are shown in fig. 14). These pressure spikes coincided with debris being ejected from the nozzle, visible in high-speed video of the motor firings.

A possible explanation of these events is that a piece of solid debris, likely char from the ablative liner, temporarily blocks the nozzle. This reduces the amount of gas which can flow out through the nozzle, causing the chamber pressure to rise. The piece of debris is then ejected, suddenly re-opening the nozzle throat and returning the chamber pressure to its normal level. The nozzle throat diameters were only ~3 mm, so even small pieces can block most of the throat area. An alternative explanation is that the pressure spikes are caused by flaws in the propellant grain which temporarily increase the burn area [30].

To survive these pressure spikes, the motor case must be designed to withstand higher pressures. A somewhat arbitrary suggestion is that the motor case's Maximum Design Pressure should be 2.0 MPa above the maximum nominal chamber pressure; 2.0 MPa is 2× the amplitude of the largest observed pressure spike. Because the nominal chamber pressure is so low, it is likely that a motor case with the minimum manufacturable wall thickness will already provide this margin.

IV. Motor testing

A research motor was developed and fired in a static test facility, using the slow-burn propellants from [9] at low chamber pressure. The low thrust / burn area levels needed for this class of motor were successfully demonstrated. These tests also measured the nozzle and combustion efficiencies, ζ_{C_F} and ζ_{c^*}, as defined in [4]. The research motor was also used to test the ablative liner and ceramic-insulated nozzle.

A. Research motor and test facility

The research motor's components are shown in fig. 12. The motor case is a round tube made from grade 2 titanium. The end-burning propellant grain burns from right to left in fig. 12; it is 40 mm in diameter. A full-length propellant grain has a mass of about 700 g, although sometimes the motor has been tested with shorter-length propellant grains. The ablative liner, 3.5 mm thick Dowsil 93-104 backed by fiberglass cloth, protects the motor case from the hot combustion gases. The motor normally uses a water-cooled nozzle (as shown in fig. 12).
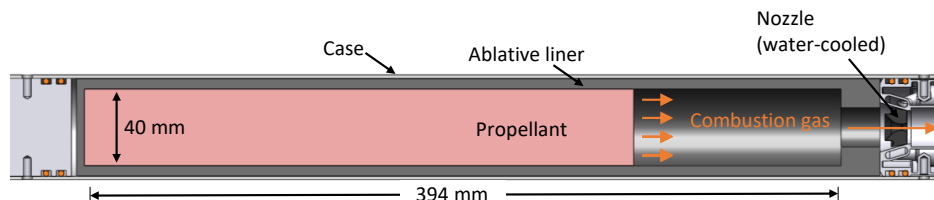

Fig. 12   Cross section of the research motor, showing the end-burn propellant grain, ablative liner, and water-cooled nozzle.

It was found that a flat face of slow-burn propellant could not be reliably ignited. Ignition was made more reliable by placing a small (2–4 g) piece of faster-burning propellant ('starter grain') into a 'starter pocket' in the aft end of the propellant grain[‖]. The starter grain was ignited by a 6 W blue laser [**] shone through the nozzle. The burning starter grain then ignited the main propellant grain around it. The additional burn area of the starter pocket causes an initial peak in chamber pressure. After the starter pocket burns away, the burning surface becomes a flat circle (with burn area $\pi(20\,\text{mm})^2 = 1257\,\text{mm}^2$) and the chamber pressure levels off at a lower value for the rest of the firing.

The research motor and its instrumentation are shown in fig. 13 (a). The motor was instrumented to measure chamber pressure, thrust, and the temperature of the motor case at several locations. Measuring very low thrust levels required a specialized thrust stand, which is described in [20], section 7.3. Table 4 lists the manufacturer's rated accuracy of each sensor, and the resolution at which it was read by the analog-to-digital converter (ADC)[††] used in these experiments. For each thermocouple, the bias was calibrated out (to within 0.1 K) using an ice-water bath before mounting the thermocouple to the motor case. All data channels were recorded at 100 Hz.

[‖]The starter pocket is not depicted in fig. 12 (as depicted in that figure it has already burned away), but is depicted in figures 7-5 and 7-6 of [20].
[**]A NUBM44 445 nm laser diode from Nichia Corp., Anan, Japan
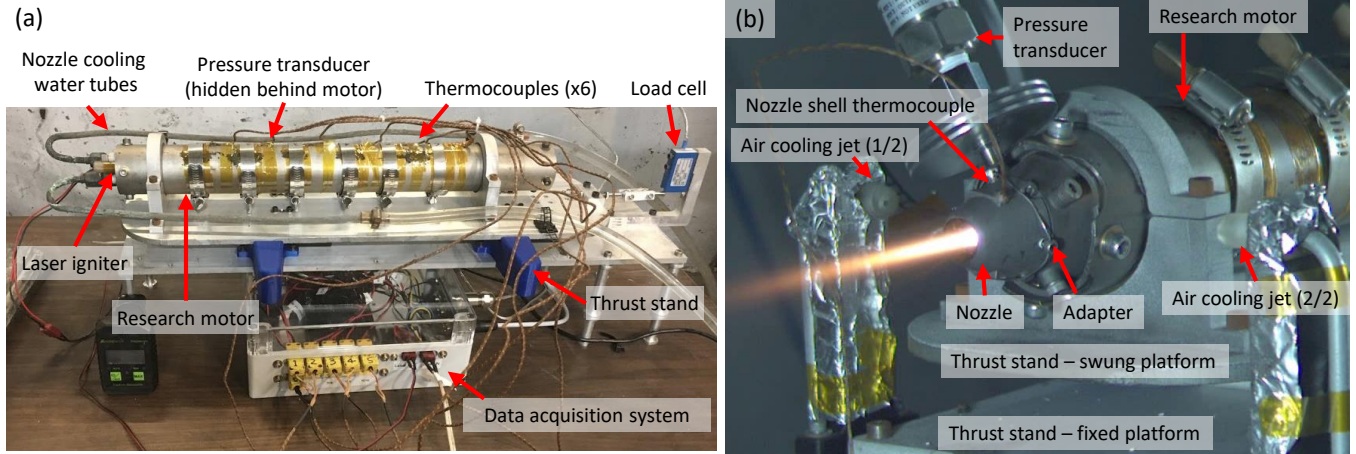[††]U3 data acquisition system from LabJack Corp., Lakewood, Colorado

Fig. 13 (a) The research motor is instrumented to measure thrust, chamber pressure and case temperatures. (b) A prototype air-cooled nozzle was tested on the research motor.

Table 4 Sensors used on the research motor. ADC accuracy is 0.13% of the full-scale range. Thermocouples and load cell use instrumentation amplifiers with 0.2% accuracy.

Sensor	Type or model	Full scale range	Sensor accuracy	ADC flicker-free resolution
Thermocouple	Type K	73–1523 K	2.2 K or 0.75% ΔT	1.25 K
Load cell	Omega LCEB-5	0–22.24 N	0.013 N	0.028 N
Pressure transducer	Omega PX119-600AI	0–4.14 MPa	0.02 MPa	0.005 MPa

The research motor was also used to test prototypes of air-cooled, ceramic-insulated nozzles discussed in section III.B, This setup is shown in fig. 13 (b). Two air cooling jets blow onto the nozzle shell to simulate the in-flight external air flow.

B. Motor testing results

Five static firings of the research motor are analyzed here; the conditions of these firing are listed in table 5. These firings were used to measure the motor's thrust coefficient and characteristic velocity, and to verify operation at low F/A_b.

1. Thrust and chamber pressure measurements

Thrust and chamber pressure measurements were recorded for all static fires (fig. 14). The thrust and pressure curves for SF-A, B and D all have a similar shape: a peak followed by a plateau. The peak is due to increased burn area just after ignition; the thrust and pressure plateau once a flat end-burn surface is achieved. SF-C used a multi-segment propellant grain. The aft (first to burn) segment contained 0% oxamide, burned faster, and produced higher chamber pressure and thrust. The front (last to burn) segment contained 10% oxamide, burned slower, and produced lower

---

‡‡Throat diameters before-after firing; the nozzle eroded during the firing.

Table 5 Firings of the research motor referenced in this section. SF-C used a multi-segment propellant grain with two different propellants.

Static fire designation	Oxamide [% by mass]	AP blend	Burn length [mm]	Cooling	Throat diam. [mm]
		——— Propellant ———		——— Nozzle ———	
SF-A	13%	400/200 μm	175	Water	2.99
SF-B	13%	400/200 μm	175	Water	3.02
SF-C seg. 1	0%	400/200 μm	182	Water	3.02
SF-C seg. 2	10%	400/200 μm	182		
SF-D	10%	400 μm	86	Air	2.82-2.95[‡‡]
SF-E	20%	400 μm	54	Air	2.08-2.28[‡‡]

chamber pressure and thrust. The multi-segment grain is described further in Mathesius [30]. SF-E had the highest oxamide content of 20%. The thrust and chamber pressure decayed during the course of the burn due to nozzle erosion and increasing heat loss to the walls as the burning propellant grain receded. The propellant self-extinguished after 54 s at a chamber pressure of approximately 0.5 MPa, near the minimum burning pressure for 20% oxamide propellant discussed further in Vernacchia *et al.* [9].

In static fires SF-A and B, there is a large amount of noise in the thrust data caused by a cooling pump mounted near the thrust stand. The cooling pump was mounted elsewhere for SF-C, and was not used in SF-D or E. In SF-A and B, the measured chamber pressure decays very slowly after burnout due to the pressure transducer plumbing becoming clogged with soot. The plumbing was modified for subsequent static fires to remedy this issue. The cause of the thrust and pressure spike at burnout in SF-A is not known.

2. Operation at low thrust / burn area ratio

A very low thrust / burn area ratio of $F/A_b = 2.4$ kPa was achieved in static fires SF-A and B. Both firings used a 13% oxamide propellant, and operated at a very low chamber pressure. The 'steady' chamber pressure (after the starter pocket transient) was 0.52 MPa in SF-A and 0.49 MPa in SF-B.

These tests were very close to the lower limit on F/A_b. Using the methods from section II.C, the lowest possible F/A_b for this propellant was predicted to be 2.7 kPa. However, this analysis assumed ideal nozzle flow. Taking into account the measured nozzle losses ($\zeta_{C_F} = 0.851$), the predicted lower limit is $F/A_b = 2.3$ kPa. Thus, SF-A and SF-B operated very close to the lowest possible F/A_b for their propellant.

Demonstrating operation at low chamber pressure, close to the F/A_b limit, is an important technology risk reduction for low-thrust motors. Other propellants and motors exhibit low-frequency combustion instability (chuffing) when operated at low chamber pressure [4]. These tests show that this slow-burn propellant can operate at very low p_c without

chuffing, which is necessary for low-thrust motors.

3. Characteristic velocity measurements

The time-averaged c^* was measured from the pressure data $p_c(t)$, the nozzle throat area A_t (average of measurements before and after firing, 0.02 mm accuracy), and the propellant grain mass m_p:

$$\langle c^* \rangle = \frac{A_t}{m_p} \int_{t_{start}}^{t_{end}} p_c(t)dt \tag{10}$$

The accuracy of the c^* measurement is estimated to be $\pm 15\,\mathrm{m\,s^{-1}}$, using the propagation of error techniques from [31].

Characteristic velocity measurements for static fires SF-A, B, D, and E are presented in fig. 15. For comparison, the ideal c^* computed from chemical equilibrium simulations is plotted as a solid black curve; curves for $\zeta_{c^*} = 0.90$ and 0.80 are also shown.

These values for ζ_{c^*} are unusually low. In larger motors, ζ_{c^*} is typically > 0.95 [4]. The low values of ζ_{c^*} are probably due to heat loss from the combustion gas to walls of the motor, as c^* is proportional to the square root of temperature at the nozzle inlet. The ζ_{c^*} values measured here agree with the gas cooling predicted by the radiation model in fig. 6.

4. Thrust coefficient measurements

The thrust coefficient C_F measures the effectiveness of the nozzle expansion process. The measured C_F is computed from the thrust recording $F(t)$, chamber pressure recording $p_c(t)$, and nozzle throat area A_t: $C_F^{meas} = F/(A_t p_c)$. The ideal value of C_F can be calculated from first principles [4]. The thrust coefficient efficiency is the ratio of the measured and ideal values: $\zeta_{C_F} = C_F^{meas}/C_F^{ideal}$.

In all tests, the ideal C_F was rather low due to low chamber pressure. The measured C_F values were even lower. For example, in SF-E, the average ζ_{C_F} was 0.924. Figure 16 shows the ideal and measured C_F vs. time during this firing [§§].

This is a fairly low value of ζ_{C_F} – in large, well-designed nozzles, ζ_{C_F} is usually > 0.95. However, the nozzles in this work are expected to have larger viscous losses due to their small size. Viscous losses are higher at lower Reynolds number; the throat Re_D for these nozzles was about 25 000 whereas typical large rocket nozzles have Re_D on the order of 10^6. These viscous losses are an unavoidable feature of small nozzles.

[§§] The measured value exceeding the ideal value at startup is an artifact due to the slower impulse response of the pressure sensor compared to the thrust sensor.
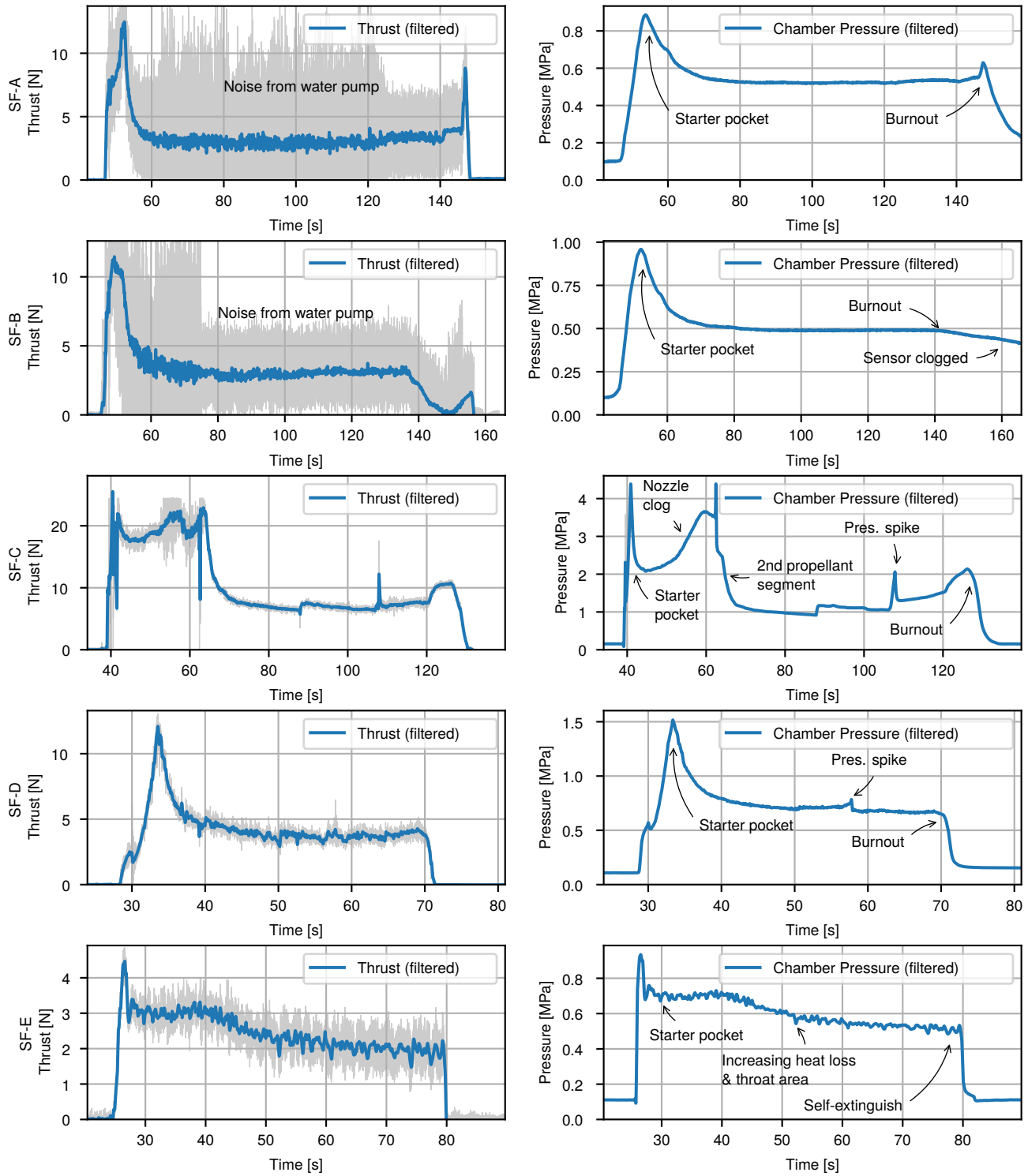
Fig. 14 Thrust (left column) and chamber pressure (right) measurements for each static fire. Raw measurements are shown in gray, the filtered signals (5 Hz low-pass, zero-phase, 5th-order Butterworth filter) are shown in blue.
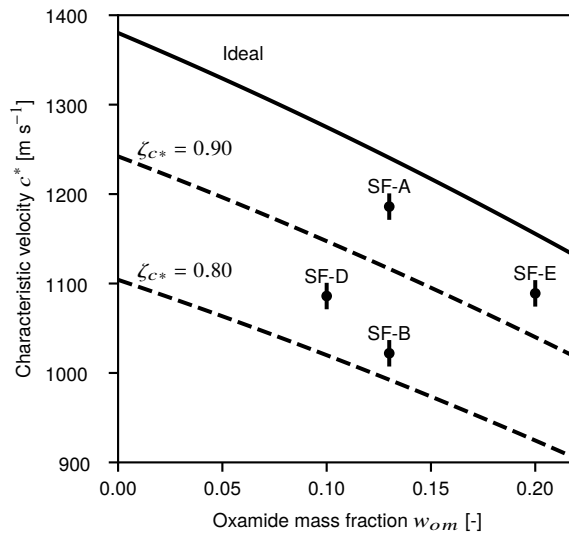
Fig. 15 Characteristic velocity measurements (with error bars) for static fires SF-A, B, D and E. These values for c^* efficiency are unusually low, probably due to energy loss from the combustion gas to the walls of the motor.
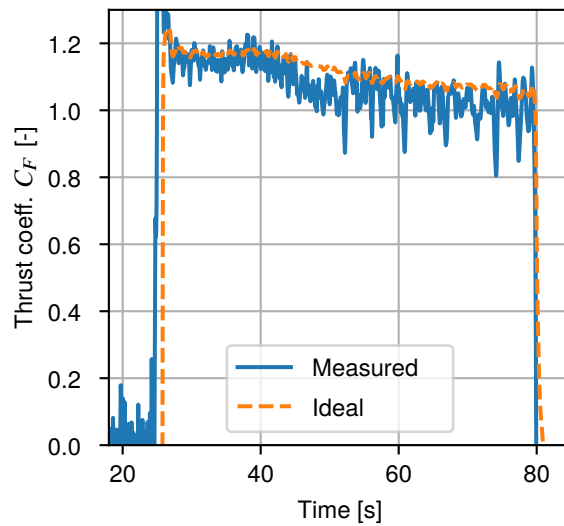

Fig. 16 In static fire SF-E, the average thrust coefficient efficiency was only 0.924.

5. Ablation and char penetration depth measurements

The char penetration depth determines the required initial thickness of the ablative liner. Thus, measurements of the char penetration depth under realistic motor conditions are important for motor design.

After static firings of the motor, the char depth was measured by cutting the liner in half and photographing the section. The liner charring is shown in fig. 17. There are two distinct regions of char: a black layer on top and a white layer beneath it. The remaining virgin (un-charred) liner material is gray.
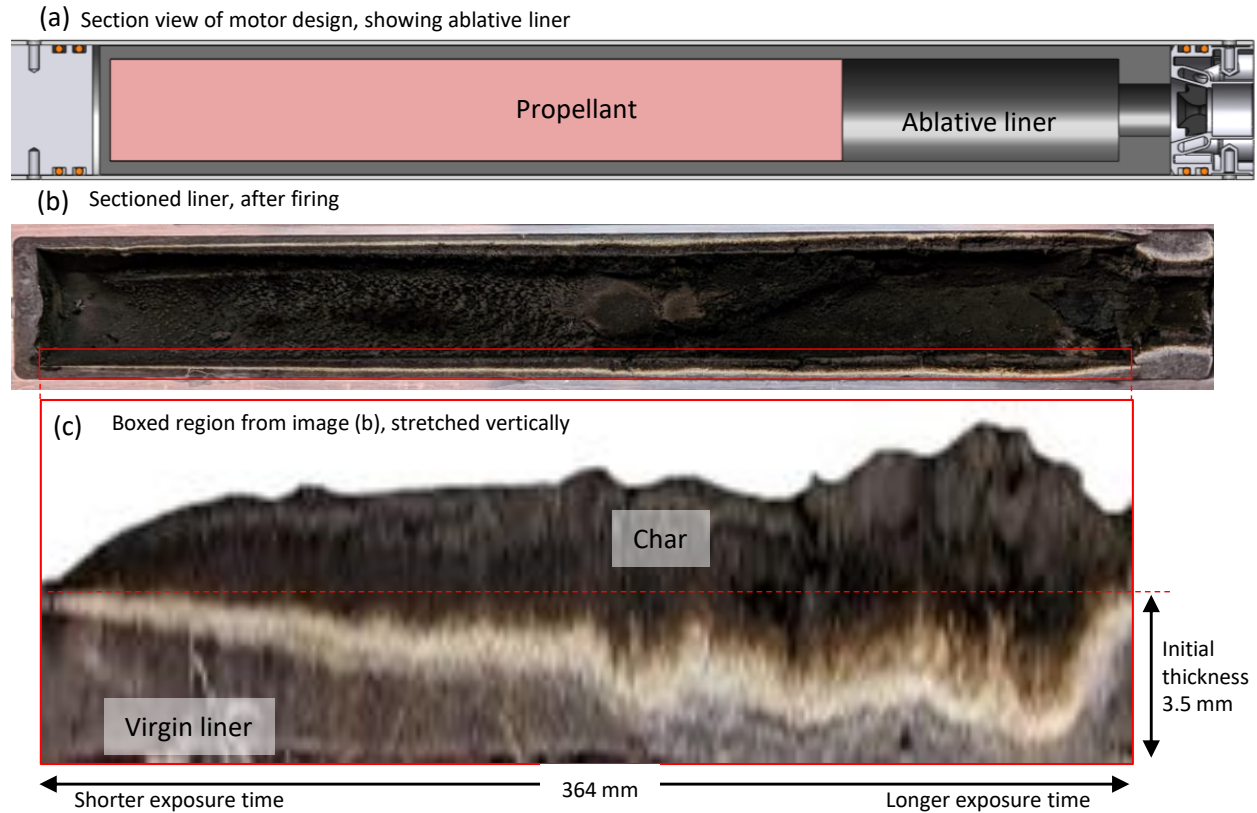

(a) Section view of motor design, showing ablative liner

(b) Sectioned liner, after firing

(c) Boxed region from image (b), stretched vertically

Fig. 17 **The ablative liner is charred by exposure to hot gas. The char has penetrated deeper where the exposure time is longer. Char also builds up beyond the initial thickness of the liner.**

The end-burning propellant grain burned from right to left in these figures, so the right side was exposed to hot gas for longer. At the right side of fig. 17(c), the char has penetrated deeper into the liner, and less virgin material remains. The char layer extends beyond the original surface of the liner (marked by a red dashed horizontal line in fig. 17(c)). This is partially due to the liner material swelling as it chars, and partially due to soot deposited on the liner from the combustion gas.

Char depth measurements for four static firings are shown in fig. 18. These firings used propellant with 10% or 13% oxamide, and had chamber pressures of 0.5–1.0 MPa. [¶¶] For two of the firings (SF-A and SF-D), two sets of

---

[¶¶]For SF-C, which used a multi-segment propellant grain, only data from the forward segment are included in fig. 18. The aft portion of the liner was exposed to combustion gases from both grain segments, so its char depth is more difficult to interpret.

depth measurements were taken, one from each side of the cut through the liner. The data show that the char depth increases *sub-linearly* with exposure time. These results indicated that this ablative liner design is feasible for small, long-burn-time motors. Despite the long burn time, the ablative liner only needs to be a few mm thick, and will not occupy an excessive amount of volume within the motor case.
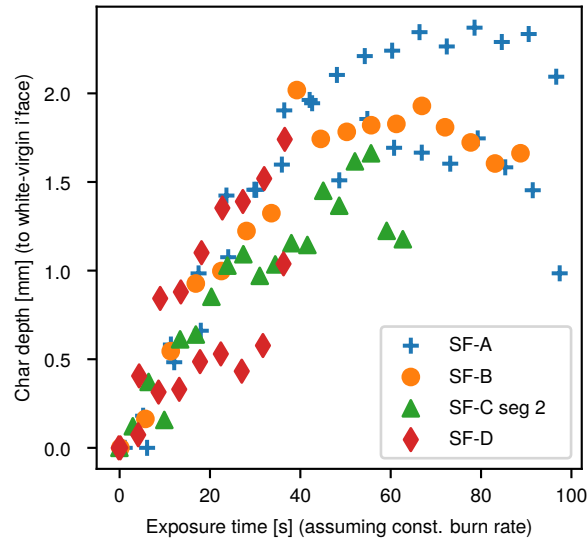

Fig. 18   Char depth measurements from four static firings show that char depth generally increases with exposure time.

6. Case temperature measurements

Six thermocouples (type K) were mounted on the outside of the motor case. The temperatures recorded during the SF-C firing are shown in fig. 19. Thermocouple TC1 was located 80 mm from the aft end of the motor; the other thermocouples were spaced forward in 50 mm increments.

The flame front passed under TC1 (the aft-most thermocouple) first; its temperature is the first to rise. There is almost no thermal conduction along the case; the thermocouples remain at the initial temperature until after the flame front passes them. Despite the long test duration (90.3 s), the case did not reach thermal steady state; its temperature was still rising at burnout. After burnout, the case temperature continued to increase as heat from the hot char soaked out to the case.

These measurements indicate that the thermal protection system performed adequately. The case temperatures recorded during the firing are well below the allowable limit for Ti-6Al-4V (810 K). The case temperature did exceed the 644 K limit of the shell-nozzle adhesive, but only did so after burnout, and after burnout that adhesive may fail without consequence. This static firing had little external airflow on the case; a separate experiment measured the external convection coefficient to be 3 W m^{-2} K^{-1}. Evaluating eqs. (6) and (7) with this $h_{external}$ value predicts an upper-limit
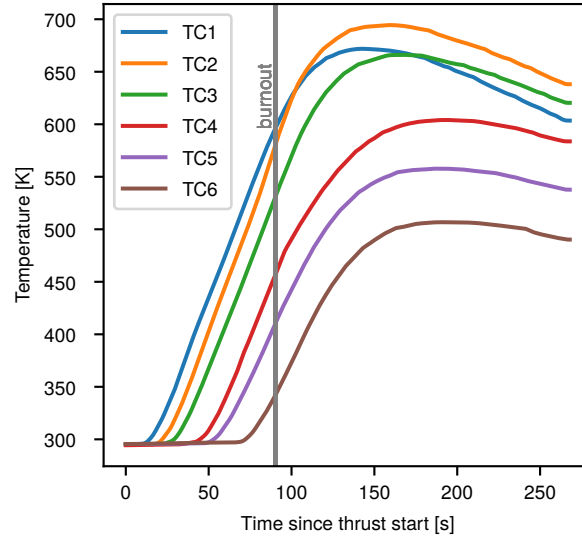
Fig. 19 **Case temperatures from static fire SF-C. The temperature of each thermocouple (TC1-6) begins to rise after the flame front passes it.**

case temperature of 683 K, just above the maximum temperature measured in SF-C. With in-flight airflow, the model predicts the case temperature could be kept below 644 K, even for longer firings that approach thermal quasi-steady state (fig. 7). This should be validated in future motor firings.

7. Nozzle demonstration

Ceramic insulated nozzles were tested on the research motor in static fires SF-D and E; the test hardware is shown in fig. 13 (b). The in-flight external convection is simulated by air cooling jets which blow on the nozzle shell. These firings demonstrated that the ceramic honeycomb insulation could withstand the period of highest thermal stress (which is expected to occur about 10 s after ignition).

These nozzle tests revealed the importance of proper material quality for the nozzle inserts. In SF-D, severe pitting of the nozzle walls was observed (see photograph in [20], fig. 9-25). Because the pitting disturbed the nozzle gas flow, the average C_F efficiency for SF-D was only 0.748. The pitting is likely due to impurities in the boron nitride material. The SF-D nozzle insert used a grade of boron nitride which contained B_2O_3 binder; this binder is not suitable for high temperatures. For SF-E a new nozzle insert was made from a 99% pure binder-less grade of boron nitride[***]. With the pure BN, no pitting occurred and the average C_F efficiency was higher, at 0.924.

As reported in table 5, the boron nitride nozzle insert's throat eroded during both firings. Some throat erosion still occurred in SF-E, even with the improved material; however the amount of erosion appears acceptable.

[***]supplied by Aremco Products Inc., Valley Cottage, New York

26

V. Conclusion

Small, fast aircraft need miniature, yet powerful, propulsion systems. Low thrust solid rocket motors can meet this need. For example, a kilogram-scale solid rocket motor could produce 5–10 N of thrust for a few minutes – this would enable a small UAV, built around the motor, to fly at Mach 0.8.

Such a motor is very different from conventional kilogram-scale solid rocket motors. The thrust level is orders of magnitude lower, and the burn time is 10–100 times longer. To design these motors, the preliminary selection of thrust, chamber pressure and propellant can be made using the charts in section II.C, and is linked to the aircraft design and mission by the thrust / burn area ratio. Three major technology challenges arise for these motors, and were investigated in this work. First, a slow-burn propellant is needed, which must operate a unusually low chamber pressures of 0.5–2 MPa. Several AP+HTPB+oxamide propellants were characterized; their burn rates can meet the needs of a range of aircraft and missions by varying the propellant's oxamide content. Second, the inner surface of the motor is exposed by the end-burn configuration and requires thermal protection. This is accomplished with a silicone-matrix ablative and fiberglass insulation, but the heat loss from the combustion gas causes a noticeable 15% reduction in impulse. Third, the millimeter-scale nozzle cannot be ablatively cooled for several minutes, and instead uses a cermaic nozzle surrounded by thermal-stress-tolerant fused silica insulation. The feasibility of all these solutions were demonstrated in motor firings.

References

[1] *Jane's All the World's Aircraft: Unmanned*. IHS Markit, London, 2016.

[2] *Jane's All the World's Aircraft: In Service*. IHS Markit, London, 2016.

[3] Lennox, D. and Rees, A., *Jane's Weapons: Air Launched*. Jane's Information Group, Alexandria, Virginia, 1988.

[4] Sutton, G. P. and Biblarz, O., *Rocket Propulsion Elements*, 8th ed. John Wiley & Sons, Inc., Hoboken, New Jersey, 2010.

[5] Shafer, J. I., "Solid-Propellant Motors for High-Incremental-Velocity Low-Acceleration Maneuvers in Space," JPL-TM-33-528, Jet Propulsion Laboratory, Pasadena, California, Mar. 1972. `https://ntrs.nasa.gov/search.jsp?R=19720012197`.

[6] Nowakowski, P., Kasztankiewicz, A., Marciniak, B., Okninski, A., Pakosz, M., Noga, T., Majewska, E., Rysak, D., and Wolanski, P., "Space Debris Mitigation Using Dedicated Solid Rocket Motor," *8th European Conference for Aeronautics and Space Sciences*, Madrid, Spain, 2019.
https://doi.org/10.13009/EUCASS2019-994.

[7] Compton, J., Thies, C., Kurzeja, S., and McGarry, J., "Five-Minute Rocket Motor," *AIAA/SAE 10th Propulsion Conference*, AIAA, San Diego, California, Oct. 1974.
https://doi.org/10.2514/6.1974-1203.

[8] Cavcar, M., "Bréguet Range Equation?" *Journal of Aircraft*, Vol. 43, No. 5, 2006, pp. 1542–1544.
https://doi.org/10.2514/1.17696.

[9] Vernacchia, M. T., Mathesius, K. J., and Hansman, R. J., "Slow-Burn Ammonium Perchlorate Composite Propellants with Oxamide: Burn Rate Model, Testing and Applications," *Journal of Propulsion and Power (not yet published)*,

[10] Vernacchia, M. T., "Development, Modeling and Testing of a Slow-Burning Solid Rocket Propulsion System," MS thesis, Massachusetts Institute of Technology, Cambridge, Massachusetts, 2017.
https://dspace.mit.edu/handle/1721.1/112515.

[11] Natali, M., Kenny, J. M., and Torre, L., "Science and Technology of Polymeric Ablative Materials for Thermal Protection Systems and Propulsion Devices: A Review," *Progress in Materials Science*, Vol. 84, Dec. 2016, pp. 192–275.
https://doi.org/10.1016/j.pmatsci.2016.08.003.

[12] Resch, C. L., "Ablation Models of Thermal Protection Materials," *Johns Hopkins APL Techincal Digest*, Vol. 13, No. 3, 1992, pp. 426–430.
https://www.jhuapl.edu/Content/techdigest/pdf/V13-N03/13-03-Resch.pdf.

[13] Moyer, C. B. and Rindal, R. A., "An analysis of the coupled chemically reacting boundary layer and charring ablator. Part 2 - Finite difference solution for the in-depth response of charring materials considering surface chemical and energy balances," NASA-CR-1061, Jun. 1968.
https://ntrs.nasa.gov/search.jsp?R=19680017220.

[14] Chen, Y.-K. and Milos, F. S., "Ablation and Thermal Response Program for Spacecraft Heatshield Analysis," *Journal of Spacecraft and Rockets*, Vol. 36, No. 3, 1999, pp. 475–483.
https://doi.org/10.2514/2.3469.

[15] Pearce, B. E., "Radiative Heat Transfer within a Solid-Propellant Rocket Motor," *Journal of Spacecraft and Rockets*, Vol. 15, No. 2, 1978, pp. 125–128.
https://doi.org/10.2514/3.28003.

[16] Duval, R., Soufiani, A., and Taine, J., "Coupled Radiation and Turbulent Multiphase Flow in an Aluminised Solid Propellant Rocket Engine," *Journal of Quantitative Spectroscopy and Radiative Transfer*, Vol. 84, No. 4, 2004, pp. 513–526.
https://doi.org/10.1016/S0022-4073(03)00268-1.

[17] Cross, P. G., "Radiative Heat Transfer in Solid Rocket Nozzles," *Journal of Spacecraft and Rockets*, Vol. 57, No. 2, 2020, pp. 247–260.
https://doi.org/10.2514/1.A34598.

[18] Hill, P. and Peterson, C., *Mechanics and Thermodynamics of Propulsion*, 2nd ed. Pearson Education, Inc., New York, 1992.

[19] Siegel, R. and Howell, J. R., "Thermal Radiation Heat Transfer: Volume 3 - Radiation Transfer with Absorbing, Emitting, and Scattering Media," NASA SP-164, Vol. 3, NASA Lewis Research Center, Cleveland, Ohio, Jan. 1971.
https://ntrs.nasa.gov/search.jsp?R=19710021465.

[20] Vernacchia, M. T., "Development of Low-Thrust Solid Rocket Motors for Small, Fast Aircraft Propulsion," Ph.D. Dissertation, Massachusetts Institute of Technology, Cambridge, Massachusetts, May 2020.
https://hdl.handle.net/1721.1/127069.

[21] Spirnak, J. R., "Development, modeling and testing of thermal protection systems in small, slow-burning solid rocket motors," Thesis, Massachusetts Institute of Technology, Cambridge, Massachusetts, 2018.
https://dspace.mit.edu/handle/1721.1/118689.

[22] "Propulsion Products Catalog," Nothrop Grumman Innovation Systems, Magna, Utah, Jun. 2018.

[23] Ellis, R. A. and Keller, R. B., "SP-8115: Solid Rocket Motor Nozzles," NASA-SP-8115, NASA Lewis Research Center, Cleveland, Ohio, Jun. 1975.
https://ntrs.nasa.gov/search.jsp?R=19760013126.

[24] Barron, R. F. and Barron, B. R., "Thick-Walled Cylinders and Spheres," *Design for Thermal Stresses*, John Wiley & Sons, Inc., Hoboken, New Jersey, 2011, pp. 378–415.
https://doi.org/10.1002/9781118093184.ch9.

[25] Kingery, W. D., "Factors Affecting Thermal Stress Resistance of Ceramic Materials," *Journal of the American Ceramic Society*, Vol. 38, No. 1, 1955, pp. 3–15.
https://doi.org/10.1111/j.1151-2916.1955.tb14545.x.

[26] Goldstein, H. E., "Fibrous Ceramic Insulation," *Advanced Materials Technology*, NASA Langley Research Center, Hampton, Virginia, Nov. 1982, pp. 261–274.
https://ntrs.nasa.gov/search.jsp?R=19830003890.

[27] Lu, T. J. and Fleck, N. A., "The Thermal Shock Resistance of Solids," *Acta Materialia*, Vol. 46, No. 13, 1998, pp. 4755–4768.
https://doi.org/10.1016/S1359-6454(98)00127-X.

[28] Wan, W., Huang, C.-e., Yang, J., Zeng, J., and Qiu, T., "Effect of Sintering Temperature on the Properties of Fused Silica Ceramics Prepared by Gelcasting," *Journal of Electronic Materials*, Vol. 43, No. 7, 2014, pp. 2566–2572.
https://doi.org/10.1007/s11664-014-3112-7.

[29] Gibson, L. J. and Ashby, M. F., *Cellular Solids: Structure and Properties*, 2nd ed., Cambridge Solid State Science Series. Cambridge University Press, Cambridge, United Kingdom, 1997.
https://doi.org/10.1017/CBO9781139878326.

[30] Mathesius, K. J., "Manufacturing Methods for a Solid Rocket Motor Propelling a Small, Fast Flight Vehicle," MS thesis, Massachusetts Institute of Technology, Cambridge, Massachusetts, Jun. 2019.
https://dspace.mit.edu/handle/1721.1/122377.

[31] "Propagation of Error for Many Variables," *NIST/SEMATECH e-Handbook of Statistical Methods*, National Institute of Standards and Technology, Gaithersburg, Maryland, Oct. 2013.
https://doi.org/10.18434/M32189.